

# Design and performance of single photon APD focal plane arrays for 3-D LADAR imaging

Mark A. Itzler\*, Mark Entwistle, Mark Owens, Ketan Patel, Xudong Jiang, Krystyna Slomkowski, and Sabbir Rangwala

*Princeton Lightwave Inc., 2555 US Route 130 S., Cranbury, NJ 08512*

Peter F. Zalud, Tom Senko, John Tower, and Joseph Ferraro  
*Sarnoff Corp., 201 Washington Road, Princeton, NJ 08543*

## ABSTRACT

We describe the design, fabrication, and performance of focal plane arrays (FPAs) for use in 3-D LADAR imaging applications requiring single photon sensitivity. These 32 x 32 FPAs provide high-efficiency single photon sensitivity for three-dimensional LADAR imaging applications at 1064 nm. Our GmAPD arrays are designed using a planar-passivated avalanche photodiode device platform with buried p-n junctions that has demonstrated excellent performance uniformity, operational stability, and long-term reliability. The core of the FPA is a chip stack formed by hybridizing the GmAPD photodiode array to a custom CMOS read-out integrated circuit (ROIC) and attaching a precision-aligned GaP microlens array (MLA) to the back-illuminated detector array. Each ROIC pixel includes an active quenching circuit governing Geiger-mode operation of the corresponding avalanche photodiode pixel as well as a pseudo-random counter to capture per-pixel time-of-flight timestamps in each frame. The FPA has been designed to operate at frame rates as high as 186 kHz for 2  $\mu$ s range gates. Effective single photon detection efficiencies as high as 40% (including all optical transmission and MLA losses) are achieved for dark count rates below 20 kHz. For these planar-geometry diffused-junction GmAPDs, isolation trenches are used to reduce crosstalk due to hot carrier luminescence effects during avalanche events, and we present details of the crosstalk performance for different operating conditions. Direct measurement of temporal probability distribution functions due to cumulative timing uncertainties of the GmAPDs and ROIC circuitry has demonstrated a FWHM timing jitter as low as 265 ps (standard deviation is  $\sim$ 100 ps).

**Keywords:** avalanche photodiodes, single photon detector, photon counting, Geiger-mode APD, LADAR, three-dimensional imaging, InP, InGaAsP

## 1. INTRODUCTION

When compared with conventional two-dimensional imaging sensors, new three-dimensional imaging technologies provide a much greater wealth of information for object recognition and identification. Many of the ambiguities present in 2-D images are eliminated by obtaining explicit high-resolution range (i.e., depth) information for details of the scene. The isolation of specific objects in intensity images must be accomplished using edge examination and complex image processing algorithms that generally require assumptions about the scene that may not be appropriate for a given set of image data. Three dimensional data remove the ambiguity of edge determination and provide more definitive information concerning imaged objects.

By employing high-resolution range measurements at each pixel of the imager, the user can obtain image data in three spatial dimensions [1,2] that enable advanced applications—such as the imaging of targets behind obscuring foliage or camouflage netting—that are not possible using traditional two-dimensional intensity images. This 3-D imaging technique works by exploiting voids in foliage, netting, or other obscuration that expose portions of objects which are otherwise veiled by these foreground elements. As the sensor platform moves, a new distribution of voids reveals additional information pertaining to the objects, and the fusion of multiple image frames allows for a high-resolution 3-D image of obscured objects to be formed.

\*mitzler@princetonlightwave.com; tel: 1.609.495.2551; www.princetonlightwave.com

This work was sponsored by the Defense Advanced Research Projects Agency under contract HR0011-08-C-0021. Approved for Public Release, Distribution Unlimited. The views, opinions, and/or findings contained in this article are those of the author and should not be interpreted as representing the official views or policies, either expressed or implied, of the Defense Advanced Research Projects Agency or the Department of Defense.

The use of short laser pulses of ns-scale duration provides much higher resolution imaging than longer wavelength sensing techniques (e.g., radar) and results in far more successful target identification and recognition. The extension of this laser radar (LADAR) 3-D imaging concept to detectors with single photon detection capability [3] provides the greatest possible sensitivity, with greatly relaxed requirements on the launched power of optical pulses necessary for less sensitive sensor technologies. The problem of blinding by early-returning photons (i.e., reflected by the foreground) can be minimized by working with sufficiently low power laser pulses so that the probability of receiving more than one photon per pixel per image frame is small. Even if few photons reflect off the object of interest and reach the 3-D imager by traversing the foreground in two passes, the ability to measure single photons allows for image data to be obtained and constitutes the most efficient use of transmitter power. By accumulating multiple frames of data at high repetition rates using low power pulses, one obtains the maximum information extraction from each photon along with good statistics for image construction based on intensity as well as range.

In this paper, we report on the design, fabrication, and performance of focal plane arrays (FPAs) for 3-D imaging systems with single photon sensitivity employing two-dimensional arrays of InGaAsP-based Geiger-mode avalanche photodiodes (GmAPDs) with high-efficiency single photon sensitivity at 1.06  $\mu\text{m}$ . The results described here represent considerable maturation of this FPA technology relative to preliminary work described in a previous publication. [4] Our GmAPD arrays employ a planar-passivated single avalanche diode device platform with buried p-n junctions that has demonstrated excellent performance uniformity, operational stability, and long-term reliability. For a typical 32 x 32 GmAPD FPA, full-array mapping for dark count rate (DCR) and photon detection efficiency (PDE) shows excellent pixel-level yield and performance. An average PDE of 35% (which includes all optical losses, including those from an integrated microlens array) is obtained for an average DCR of 15 kHz, with all pixels except one exhibiting less than 26 kHz DCR. Crosstalk characterization shows that the largest per-pixel crosstalk contribution comes from nearest neighbor pixels and is less than 1% at operating conditions that provide 35% PDE. We also describe an over-sampling technique that allows us to directly measure the probability distribution function (PDF) of the timing of photon detection events. Using the width of this PDF to determine the FPA timing jitter, a FWHM criterion yields  $\sim 265$  ps and a standard deviation criterion yields  $\sim 100$  ps.

## 2. GEIGER-MODE APD FOCAL PLANE ARRAY DESIGN ELEMENTS

The GmAPD FPA module described in this paper is comprised of a number of critical sub-components, including a photodiode array (PDA) based on GmAPD pixels; a readout integrated circuit (ROIC) for pixel-level electrical interfacing and FPA-level control; a GaP microlens array (MLA) to ensure high fill factor; and various packaging sub-components to define electrical, mechanical, and optical interfaces to the overall module. To enable turnkey operation of the module using a standard personal computer, we have also designed an FPGA-based evaluation interface board. In this section, we discuss the design of the PDA, the ROIC, the overall module construction, and the interface board.

### 2.1 Geiger-mode APD photodiode array (PDA)

When an avalanche photodiode is biased above its breakdown voltage  $V_b$ , the photoexcitation of a single electron-hole pair by a single photon can induce a run-away avalanche that gives rise to a detectable macroscopic pulse of current. In this mode of operation, usually referred to as Geiger mode, the detection of the avalanche current pulse by appropriate electrical circuitry can signal the arrival of just a single photon. (For this reason, these detectors are also often referred to as single photon avalanche diodes, or SPADs.) Our 1.06  $\mu\text{m}$  Geiger-mode avalanche diode (GmAPD) device design shares similarities with InP/InGaAs GmAPDs designs that we have employed for longer wavelength operation with a 1.67  $\mu\text{m}$  room-temperature cutoff [5]. In previous publications [5 – 10], we have described in detail the design, simulation, and characterization of discrete GmAPD devices employing both InGaAs and InGaAsP absorption regions. Unlike linear mode APDs operated below  $V_b$ , the GmAPD detection process is inherently digital, and with appropriately designed detectors and threshold circuits, the Geiger-mode detection process is noiseless.

#### 2.1.1 Discrete GmAPD devices

To create focal plane arrays (FPAs) with single-photon sensitivity at every pixel, we have employed our GmAPD discrete device design in an array format. In this paper, we describe FPAs with a 32 x 32 format on a 100  $\mu\text{m}$  pixel pitch. A detailed schematic cross-section of the pixel-level device structure is illustrated in Figure 1(a). The quaternary InGaAsP absorption layer with a bandgap of  $E_g \sim 1.03$  eV is lattice-matched to InP and optimized for detection of 1.06

$\mu\text{m}$  photons at an operating temperature in the range  $\sim 240 - 260$  K. The InP multiplication region has a wider bandgap of  $E_g \sim 1.35$  eV and is the region of the structure in which avalanche multiplication occurs. The spatial separation of the absorption and multiplication functions is a primary goal of this so-called “separate absorption and multiplication” (SAM) region structure [11], which maintains a low electric field in the narrower bandgap absorber (to suppress dark carriers due to tunneling) while creating a sufficiently high electric field in the multiplication region (so that impact ionization leads to avalanche multiplication). The doped “charge” layer between the absorption and multiplication regions (the SACM structure [12]) allows for more flexible tailoring of the internal electric field profile, along with the associated avalanche process, and the resulting internal electric field profile is illustrated qualitatively at the right of Figure 1(a). Grading layers between the InGaAsP and InP layers are added to mitigate hole trapping effects that result from the valence band offset that arises in an abrupt heterojunction of InGaAsP and InP [13].

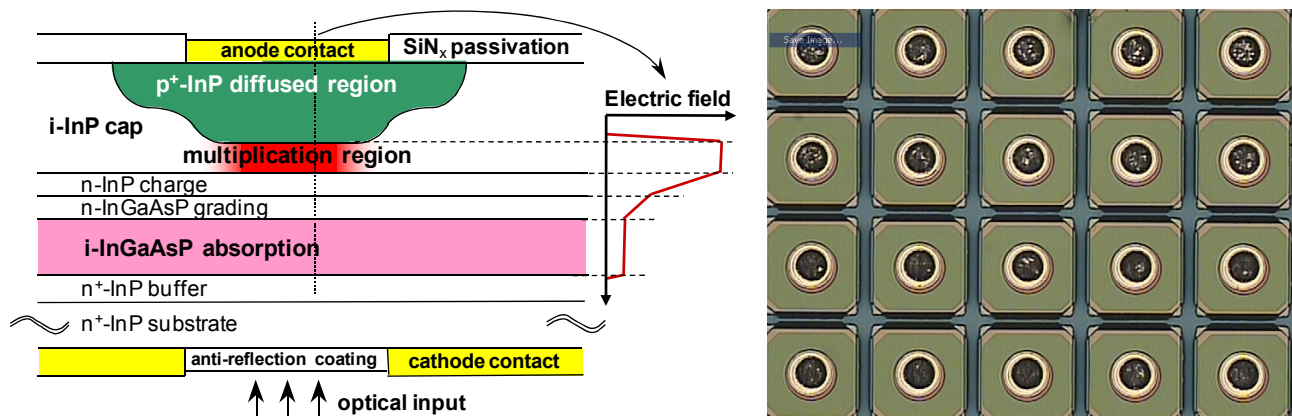


**Figure 1.** (a) Schematic cross-section of  $1.06 \mu\text{m}$  planar-geometry diffused-junction GmAPD device structure. Photons are absorbed in the InGaAsP absorption layer, and photoexcited holes are injected into the high-field multiplication region which provides Geiger-mode avalanche gain. (b) Micrograph of fabricated GmAPD pixels showing indium bumps at center of each pixel and etched trenches between pixel active areas.

The lateral structure of our GmAPD device design employs a buried p-n junction to guarantee edge breakdown suppression, low perimeter leakage, and high reliability. The device active area is determined by the patterning of a SiN dielectric passivation layer to create a diffusion mask. A subsequent diffusion of Zn dopant atoms creates a  $\text{p}^+$ -InP region within the i-InP cap layer [see Figure 1(a)]. The quasi-cylindrical junction that is formed by a single diffusion tends to exhibit electric field enhancement where the junction curvature is large and can lead to premature avalanche breakdown at the edges of the device. To suppress this edge breakdown phenomenon, we use two diffusions to tailor the junction profile [14] so that the junction is deeper in the central part of the active area than it is in the junction periphery. This design ensures that the gain profile across the center part of the active region is uniform and that the electric field—and therefore the gain—is reduced in the peripheral region of the device. For the arrays described in this paper, the optical active region diameter in each pixel is  $34 \mu\text{m}$ . With this buried junction design, the formation of a high-quality SiN passivation layer can provide low perimeter leakage and stable long-life performance [15].

### 2.1.2 GmAPD photodiode arrays

In the fabrication of arrays of GmAPD devices, a key consideration that does not play a role in discrete device performance is that of optical crosstalk. An avalanche of electrical carriers in one pixel gives rise to hot carrier luminescence, and even if the number of emitted photons is small (previous studies indicate 1 emitted photon for every  $\sim 10^5$  to  $10^6$  avalanche carriers), the single photon sensitivity of neighboring pixels makes them susceptible to correlated crosstalk counts triggered by these luminescence photons. To reduce the line-of-sight coupling between nearest-neighbor pixels, we have etched isolation trenches along the pixel boundaries. A micrograph of a small section of a fully fabricated GmAPD photodiode array (PDA) is shown in Figure 1(b). The GmAPD array fabrication also includes back-side anti-reflection-coated apertures aligned to the pixel active regions and front-side patterning of indium bumps to facilitate hybridization of the detectors to mating  $32 \times 32$  CMOS ROICs, described in the next sub-section.

Arrays of related mesa-geometry InP-based GmAPD have been extensively studied in pioneering work by researchers at MIT-Lincoln Laboratory [16 – 18], and significant additional work on mesa-geometry devices has also been recently reported. [19,20]. These devices are based on an epitaxial structure similar to that used for our planar geometry devices. However, instead of using dopant diffusions to define the active region p-n junctions, mesa-geometry devices have p-n junctions that are epitaxially grown, and their active areas are defined by the etching of mesas in which all epi-grown material is removed outside the intended active region. The control of edge breakdown effects in mesa-geometry devices requires a slightly beveled structure, and to accomplish this geometry, the GmAPD structure is grown on p-type InP substrates and has a dopant polarity opposite to that of our planar-geometry devices.

### 2.1.3 GmAPD device modeling

To optimize avalanche diode structures for Geiger mode operation, we have carried out extensive device modeling reported in previous publications [7,9]. In this simulational work, we adopted a formalism first described by Donnelly, et al. [17] for the calculation of photon detection efficiency (PDE) and dark count rate (DCR). The computation of PDE for specific structures requires calculations of the avalanche probability in the multiplication region under specific operating conditions—most importantly, excess bias voltage and temperature—as well as the quantum efficiency of the absorption region. DCR calculations rely on accurate descriptions of dark carrier creation, and we have found that the two most critical mechanisms impacting DCR are thermal generation of carriers in the smaller bandgap InGaAsP absorption region and tunneling effects in the high-field InP multiplication region.

Among the various structural modifications identified for Geiger-mode performance optimization, the use of wider multiplication regions has been found to be critical. In Figure 2, we illustrate the calculated dependence of DCR per unit area on the photon detection efficiency for several different values of the width of the multiplication region,  $W_m$ . Larger values of  $W_m$  provide a dramatic reduction in DCR for any given value of PDE. It is interesting to note that this design requirement for wider  $W_m$  contradicts established design rules for linear mode APDs in applications such as high-speed optical communications. [15] In linear mode APDs, smaller values of  $W_m$  on the order of 0.5  $\mu\text{m}$  or less are desirable because they provide higher gain-bandwidth products and reduced excess noise. However, high frequency response and low excess noise are essentially irrelevant to Geiger-mode operation. Therefore, high performance GmAPDs employ much wider multiplication regions, with  $W_m$  typically on the order of 1.5  $\mu\text{m}$ . Although even larger values of  $W_m$  can provide additional reduction in DCR (see Figure 2), there are trade-offs involving much higher breakdown voltages (e.g., > 100 V) and the requirement for larger excess biases (e.g., > 10 V) to achieve target PDE values.

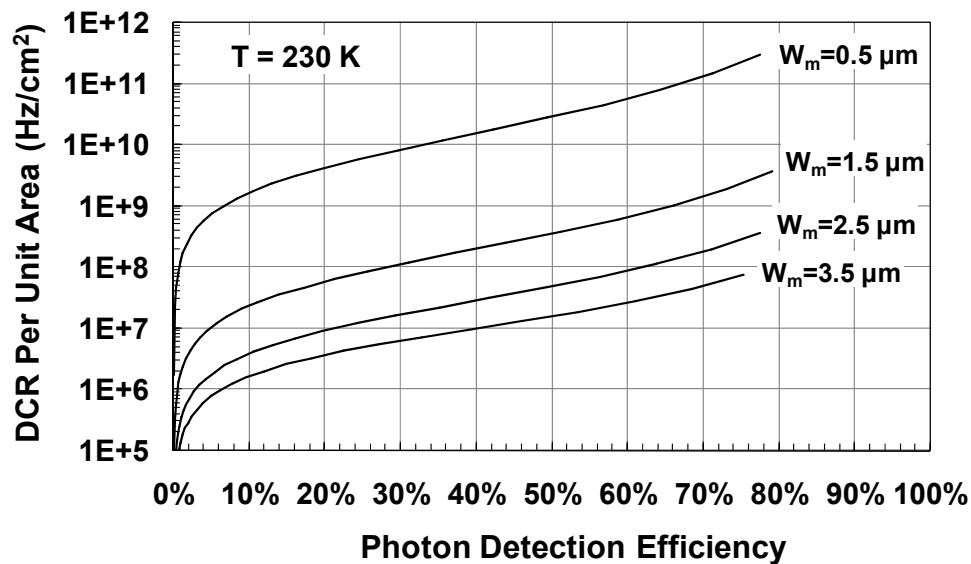


**Figure 2.** Simulation results for dark count rate (DCR) per unit area vs. photon detection efficiency for GmAPD device structures with different multiplication widths  $W_m$  at an assumed operating temperature of 230 K (Ref. [9]).

## 2.2 Readout integrated circuits (ROICs) design and functionality

The basic functions of our 3-D imaging FPA are performed by a custom CMOS ROIC mated to the GmAPD PDA by indium bump hybridization. In the disarmed state, every pixel of the detector array is biased slightly below the breakdown voltage of the GmAPD using a single external low-noise voltage supply with voltages on the order of 70 to 80 V. Each imaging frame begins with the arming of all of the detector pixels by the ROIC, which applies an excess bias of up to 5 V. The period during which the pixels remained armed is the range gate, which is typically on the order of a few microseconds. In a LADAR imaging system, the beginning of the range gate is synchronized (perhaps up to a fixed delay) with the launch of an optical pulse from which reflected photons will be detected. Every pixel contains a pseudorandom counter that provides detection timing information on a per-pixel basis. Upon asserted the master clock enable (MCE) signal, all pixel counters begin counting. Within each ROIC pixel, there is a threshold detection circuit that is triggered when an avalanche event occurs in the corresponding armed pixel of the photodiode array. When a detection occurs, an active quenching circuit removes the excess bias from the fired GmAPD pixel to disarm it, and the in-pixel counter is stopped so that the time of detection within the range gate is recorded. At the end of each range gate, pixels that do not sense an avalanche event record the terminal counter value, indicating that no event has occurred at that pixel during that image frame. The frame readout then consists of scanning out all of the pixel counter values. This FPA architecture provides range resolution corresponding to the timing resolution of the pixel counters, whereas the intensity resolution is one bit per frame since each pixel can return only a single time-stamp value per frame. Intensity information within the 3-D image data is obtained by accumulating multiple frames.

The ROIC incorporates a phase lock loop (PLL) circuit to generate highly stable clock signals for all timing operations. An overall 13-bit timing resolution is obtained using 11-bit pseudorandom counters with two additional vernier bits created by using a copy of the clock with a 90 degree phase shift. [3,18]. At the end of each range gate, frame data is scanned out using dedicated I/O ports for each of the 32 rows in the array, and high-speed scan circuitry achieves the read-out of the 32 pixels in each row in approximately 3.36  $\mu$ s. With a typical range gate duration of 2  $\mu$ s, the full frame duration of 5.36  $\mu$ s corresponds to a very high frame rate of 186 kHz. The range gate duration is user-selectable and can have any value between 1 ns and 2  $\mu$ s. For very short (i.e., ns scale) range gates, the frame rate is determined entirely by the 3.36  $\mu$ s readout and is on the order of 300 kHz. In addition to the internally supplied clock, the FPA can also be run with an external clock input if desired for system synchronization.

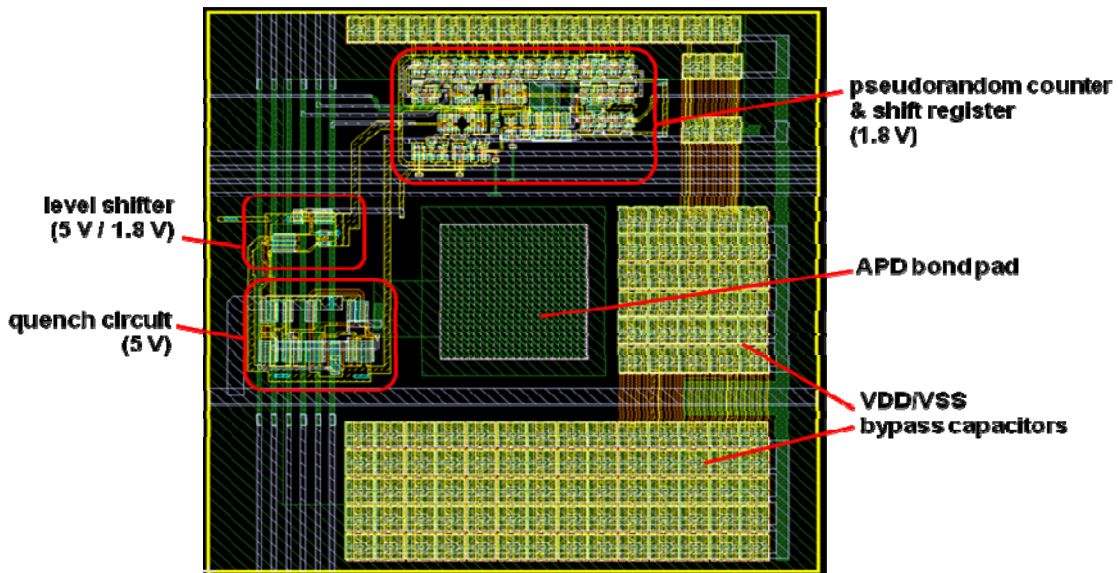


**Figure 3.** Schematic electrical layout of 100  $\mu$ m pitch pixel in ROIC. Circuitry was designed using a 0.18  $\mu$ m CMOS technology (with intentional under-utilization of the 100  $\mu$ m pitch real estate) so that identical circuits could fit within a 50  $\mu$ m pitch pixel developed for 32 x 128 format FPAs.

The design strategy of the pixel-level circuitry for this ROIC emphasized forward compatibility with a next generation of higher resolution 50  $\mu\text{m}$  pitch 32 x 128 FPAs currently under development. Scaling considerations dictated the use of a 0.18  $\mu\text{m}$  CMOS technology as well as the use of the very space-efficient pseudorandom counter in each pixel. As can be seen in the pixel-level schematic electrical layout in Figure 3, the fundamental blocks of pixel circuitry—the 1.8 V pseudorandom counter and shift register, the 5 V quenching circuit, a 1.8 V to 5 V level shifter, and the APD bond pad—occupy a relatively small fraction of the total pixel area and can be readily accommodated in a 50  $\mu\text{m}$  pitch geometry.

The ROIC design also targeted minimal power dissipation, and for conventional 3-D imaging frame rates on the order of 20 kHz, the ROIC dissipates less than 40 mW. As seen in Figure 4, which illustrates ROIC power dissipation as a function of frame rate, even for frame rates as high as 200 kHz (achieved by using range gates of slightly less than 2  $\mu\text{s}$  duration), the power dissipation is only  $\sim$ 320 mW. The power dissipation of the entire FPA module is therefore dominated by the dissipation of the integrated two-stage thermoelectric cooler incurred in establishing the required temperature differential  $\Delta T$  between the ambient case temperature and the operating temperature of the hybridized chip stack. The thermal design of the FPA will support  $\Delta T$  up to 55°C, and to operate the FPA with the PDA chip at -35°C, the FPA module dissipates about 5 W.

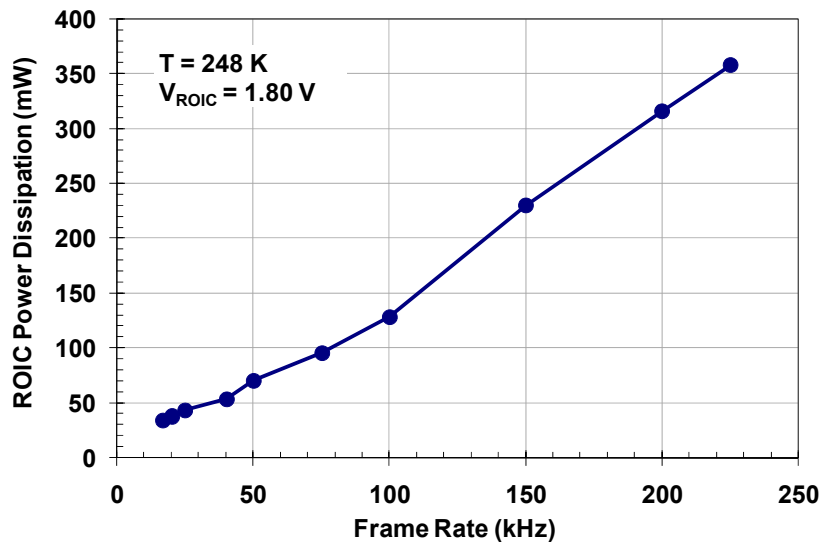


**Figure 4.** Measured ROIC power dissipation as a function of frame rate for FPA frame rates as high as 225 kHz.

### 2.3 Package assembly design

The FPA package assembly manages all of the electrical, thermal, and optical interface requirements of the FPA module. The solid body model in Figure 5(a) illustrates the principal elements of the packaged module, including a ceramic interposer board for electrical routing of the signals from the ROIC, a two-stage thermoelectric cooler (TEC) and temperature sensor, a pin grid array (PGA) ceramic housing with CuW heat sink, and a hermetically sealable lid with an anti-reflection coated sapphire window.

Following the hybridization of the GmAPD photodiode array (PDA) to the CMOS ROIC, we align and attach a GaP microlens array (MLA) to the exposed back surface of the PDA. We have developed a passive alignment technique employing matched vernier alignment fiducials on the PDA and MLA that provides for micron-scale alignment of the MLA to the PDA active areas. A high-performance optical epoxy is used to attach the MLA to the PDA with relatively rapid curing, and the process has been confirmed to be robust with respect to elimination of possible shifting of the MLA position after alignment. Based on the characterization of FPA pixel-level photon detection efficiency before and after MLA attachment, we estimate that the effective fill factor for broad illumination of the FPA is  $\sim$ 75%. (Note that the fill factor in the absence of the MLA is given by the ratio of the 34  $\mu\text{m}$  diameter GmAPD active region to the 100  $\mu\text{m}$  pitch pixel area, or  $\sim$ 9%.)

Once the MLA has been attached to the PDA, the resulting chip stack of ROIC+PDA+MLA is attached to the ceramic interposer. The photograph in Figure 5(b) shows a fully wire-bonded chip stack-on-interposer assembly, where the array structure is apparent from the lensed top surface of the MLA. The interposer is then placed on the TEC, which has been previously mounted to the ceramic housing along with the CuW heat sink. The ceramic housing includes a pin grid array with 175 pins for electrical connections. As with the ROIC design, the design of this housing incorporated elements to ensure forward compatibility with future FPA generations, including sufficient pins for ROICs with a larger number of I/O connections.

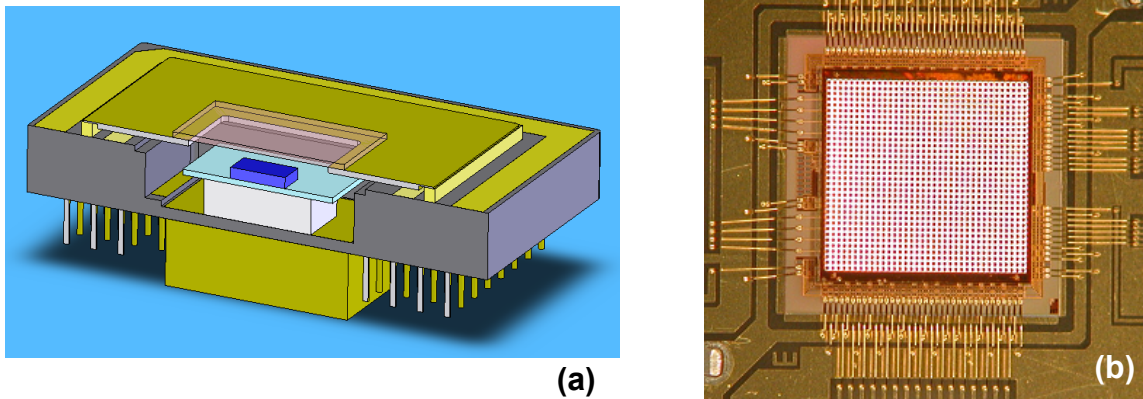


**Figure 5.** (a) Solid body model of GmAPD FPA module with cut-away showing, from bottom to top, CuW heatsink (gold), ceramic package (gray), thermoelectric cooler (white), interposer with electrical routing (light blue), hybridized PDA+ROIC+MLA chip stack (dark blue), and package window. (b) Detailed photograph of fully assembled PDA+ROIC+MLA chip stack on interposer board. The array format is apparent from the microlens array (MLA) geometry at the top of the chip stack.

## 2.4 FPGA evaluation interface board

To provide for turn-key operation of the FPA with camera-level functionality, we have designed an interface board to enable all features of the FPA and manage interfaces with support instrumentation. Primary interface board functions are managed by an Altera Cyclone III FPGA and include: FPA clock generation and scaling; data de-convolution, buffering, and high-speed output to a digital I/O card; programmable timing and pulse width of FPA control signals; device configuration registers; and laser trigger output. This board manages real-time data retrieval for the FPA, and the FPGA executes all required buffering and formatting of the pseudorandom counter timestamp data obtained from the FPA. The board also has simple electrical connections for support instrumentation (specifically, a high-voltage power supply to provide the APD bias voltage and a standard TEC controller). The board is operated by a comprehensive graphical user interface on a personal computer, and communication between the board and the computer is via National Instruments digital I/O cards.

## 3. CHARACTERIZATION OF DARK COUNT RATE AND PHOTON DETECTION EFFICIENCY

The most important characteristic of the GmAPD FPA is the fundamental tradeoff between DCR and PDE. Higher PDE can be achieved by operating the GmAPD array pixels at higher excess bias voltage, but only at the expense of increased DCR. The optimal operating point for managing this trade-off will depend on various factors dictated by the specific imaging application. As an example, for operation with high background count rates (such as daytime imaging), higher dark count rates will be tolerable as long as they do not exceed the background count rate. In this case, FPA operation with higher PDE will be desirable since the accompanying increase in DCR will not negatively impact image quality (i.e., as long as it remains background-limited). Conversely, in dark conditions with no background, DCR will dominate the noise performance of the FPA, and a different operating point for PDE may be optimal.

In this section, we demonstrate FPA data for DCR and PDE captured from the entire 32 x 32 array. We also show the distribution of DCR at a typical operating excess bias as well as the dependence of DCR on PDE for various pixels across the array.

### 3.1 Focal plane array test conditions

FPA's were characterized in a dark enclosure using the interface board described above in sub-section 2.4. Fixturing within the enclosure provided for array illumination at 1.06  $\mu\text{m}$ . PDE measurements could be obtained with optical pulses focused to a single pixel or using broad illumination that uniformly filled the entire 32 x 32 array. Single-pixel measurements were facilitated by an automated three-axis translation system used to scan the focused output of an optical fiber with translations as small as 1  $\mu\text{m}$ . For measurements taken on arrays prior to microlens array attachment, the focused beam was adequately narrow (8  $\mu\text{m}$  at the  $1/e^2$  points) at the plane of the array to confirm that the effective diameter of the active region was 34  $\mu\text{m}$  to within an uncertainty of  $\pm 2$   $\mu\text{m}$ . For array-level PDE characterization under broad illumination, the fiber source was backed away from the FPA and collimated so that the optical intensity variation across the array was no more than  $\pm 5\%$ . DCR measurements were obtained with no illumination.

Measurements reported in this section were taken with the FPA case temperature at  $\sim 293$  K and the GmAPD PDA stabilized at 248 K using the two-stage TEC integrated into the hermetic FPA module. Data could be obtained as a function of excess bias voltage, and data presented below represent excess bias values up to 4.0 V. Illuminated measurements were made using a pulsed 1.06  $\mu\text{m}$  laser with a pulse width of  $\sim 170$  ps. The optical pulse timing could be set to have pulse arrivals at any point within the 2  $\mu\text{s}$  range gate, and most data was acquired with pulse arrivals near the midpoint of the range gate (i.e., for counts corresponding to  $\sim 1$   $\mu\text{s}$ ). For single pixel measurements, the pulse intensity was typically attenuated to a mean photon number of  $\eta = 0.1$  so that the Poisson probability of there being two photons in any given pulse was less than 1%. For some measurements,  $\eta = 1$  was used to increase the data acquisition rate, in which case the resulting illuminated count measurements were corrected by assuming Poisson statistics to arrive at the intrinsic PDE. To reduce statistical uncertainty in DCR and PDE measurements, the data presented below are based on the collection of between 10,000 and 25,000 frames of data.

### 3.2 DCR and PDE performance maps

The most fundamental characterization of the FPA performance consists of maps of all 1024 pixels for DCR and PDE. The map in Figure 6(a) illustrates FPA DCR performance, with the quantitative value of DCR for each pixel indicated in kHz. The map in Figure 6(b) illustrates PDE performance, with quantitative values for each pixel indicated in percentage (%). These data demonstrate excellent yield, including 100% hybridization (i.e., all connections between PDA and ROIC are present), and just one pixel exhibiting DCR above 26 kHz [at position (9,31)].

The average PDE for the array—excluding the one out-of-spec pixel at location (9,31)—is 35%, and the standard deviation of the distribution of PDE values is 5.8%. The DCR distribution for the entire array, which has an average of 15.3 kHz and a standard deviation of 4.2 kHz (excluding the one out-of-spec pixel), is illustrated in more detail in Figure 7. From the maps in Figure 6, it is apparent that variation in DCR and PDE across the array is quite smooth, with very little random fluctuation. This suggests that non-uniformities are the result of systematic variation in device properties, with the most important factor being the variation in breakdown voltage  $V_b$ . Since a single applied voltage  $V_a$  is supplied to the entire array, the excess bias  $V_{\text{ex}} = V_a - V_b$  will vary among different pixels if they have different values of  $V_b$ . A smaller  $V_{\text{ex}}$  will result in smaller values for both DCR and PDE, and we see that the two variables tend to trend together at different locations across the array.

Non-uniformities in  $V_b$  arise from two basic contributions. Epitaxial growth non-uniformities generally contribute to wafer-scale gradients in pixel characteristics and tend to impose modest monotonic variations across the  $\sim 3$  mm scale of the each individual PDA. Process variations can have a more local impact and are most likely to be responsible for the tendency towards lower DCR and PDE near the edges of the array. Although more rare, local epitaxial variations can also lead to isolated local non-uniformities, such as those seen at pixels (10,19) and (11,19); in this case, a local variation leading to high  $V_b$  results in locally reduced values for both DCR and PDE. Other sources of performance variation are also possible and may affect DCR and PDE differently. For instance, the rotational misalignment of the microlens array lenses relative to the PDA active areas can induce gradients in the PDE performance but has no impact on the DCR values.

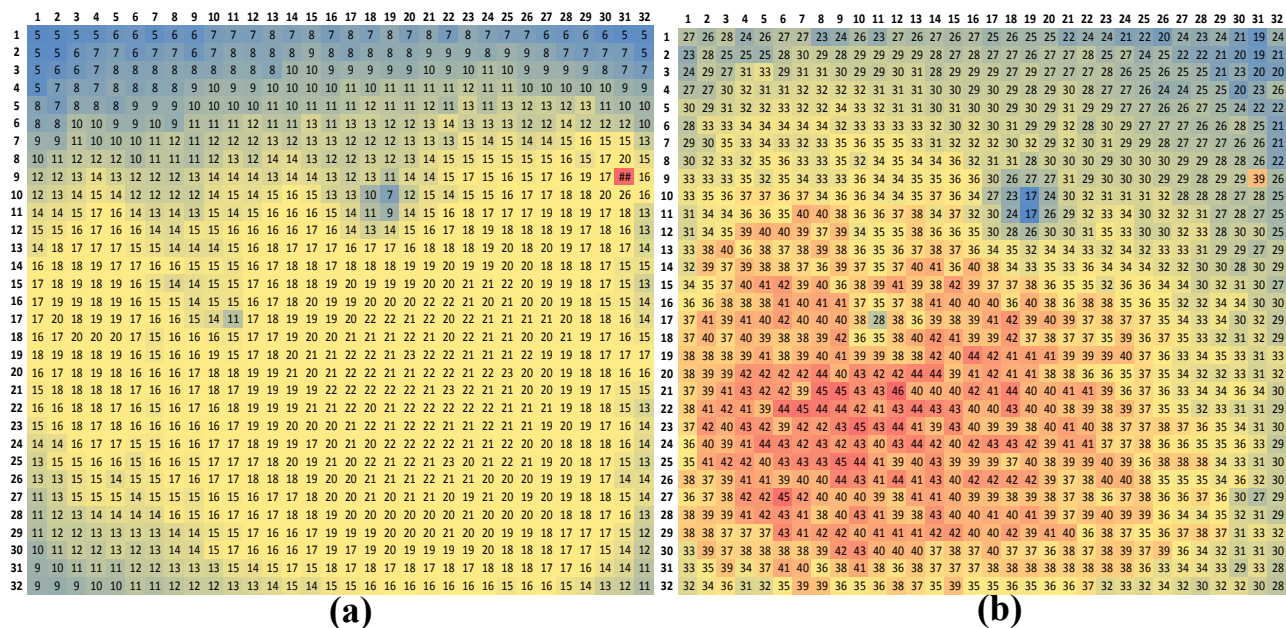


**Figure 6.** Performance maps of all 1024 pixels of a 32 x 32 GmAPD FPA operating with an excess bias of 3.5 V at 248 K. (a) Dark count rate (DCR) in kHz for all pixels, with just one out-of-spec pixel at position (9,31). (b) Photon detection efficiency (PDE) in % for all pixels, where the average pixel PDE of 35% includes all optical losses related to the microlens array and other sources of insertion loss.

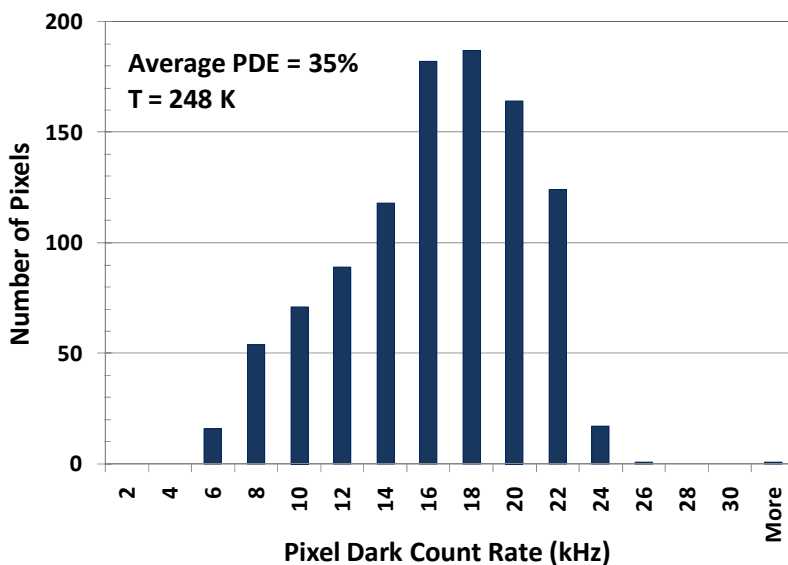


**Figure 7.** Histogram of pixel dark count rates for the DCR map data presented in Figure 6. Excluding the single pixel with a high dark count rate, the DCR distribution at 248 K has an average of 15.3 kHz with a standard deviation of 4.2 kHz. Data were obtained at an excess bias of 3.5 V, which corresponds to an average PDE of 35%.

We note that the non-uniformity in PDE giving can be easily corrected using non-uniformity correction factors. However, in many applications, the FPA is scanned within the scene being imaged, and the scanning tends to remove the impact of PDE non-uniformity without additional correction.

### 3.3 DCR vs. PDE as a function of excess bias voltage

As described earlier, the relationship between DCR and PDE presents the most fundamental tradeoff in GmAPD operation. To illustrate this relationship in more detail, we have plotted in Figure 8 the dependence of DCR on PDE for a random selection of pixels across the array. Although there is some variation among these pixels, at any given value of PDE, they all exhibit DCR values within a factor of  $\sim 2$  of the average performance indicated by the dashed curve. Each point on a DCR vs. PDE curve is obtained by measuring these two parameters at a single value of the excess bias. The collection of DCR vs. PDE curves in Figure 8 shows more consistent behavior than is apparent in the full-array performance maps in Figure 7 because the maps include the additional variation imposed by non-uniformities in  $V_b$  (and therefore  $V_{ex}$ ).

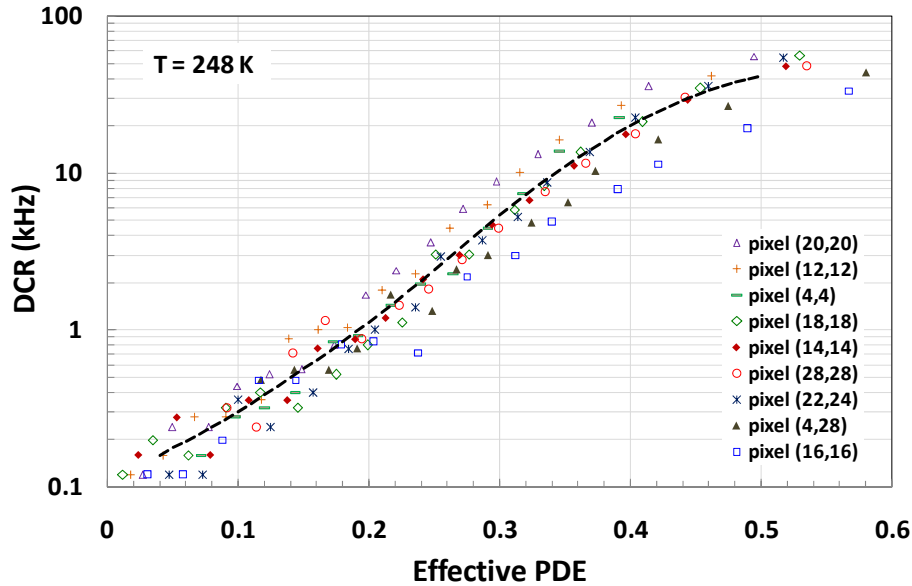


**Figure 8.** Dependence of DCR on the effective PDE for a random sample of pixels from the performance maps presented in Figure 6. The dashed line is a heuristic polynomial fit intended to show average pixel performance.

## 4. CHARACTERIZATION OF CROSSTALK BEHAVIOR

When avalanches occur in a GmAPD, the acceleration of electrical charges in the high-field avalanche region can result in the emission of photons. This hot carrier luminescence effect creates only a small number of photons—on the order of one photon for every  $10^5$  to  $10^6$  carriers—but because the pixels of a GmAPD FPA are sensitive to single photons, even a small number of emitted photons can lead to significant optical crosstalk effects if these photons are detected at neighboring pixels.

The first design imperative for minimizing crosstalk is to limit avalanche events to a relatively small number of carriers since fewer avalanche carriers will emit fewer photons due to luminescence. Accomplishing this goal relies on minimizing parasitic capacitances that are discharged with each avalanche event and pixel-level circuit design in the ROIC that limits current flow associated with detection events. A second strategy that can be employed for crosstalk reduction is the incorporation of structures within the array design that prevent emitted photons from reaching neighboring pixels. The etched trenches fabricated between neighboring pixels in our planar-geometry GmAPD PDAs [see Figure 1(b)] are an example of such a structure and significantly reduce the crosstalk between nearest neighbor pixels in our arrays.

## 4.1 Crosstalk evaluation method and performance metrics

The quantitative assessment of crosstalk behavior in our GmAPD FPAs consists of the identification of avalanche events that are temporally and spatially correlated. Because our FPA provides precise timestamp data for each avalanche event, it is straightforward to analyze frame data for temporal correlations. For each pixel of the array at which an avalanche occurred—let us call the timestamp and position of this primary avalanche  $T_0$  and  $(X_0, Y_0)$ , respectively—we search all other pixels in the vicinity of  $(X_0, Y_0)$  for avalanches that have occurred in the time interval between  $T_0$  and  $\Delta T$ . We have found that the probability of correlated avalanches for  $\Delta T > 10$  ns is negligible. There is also the probability that uncorrelated dark counts could be mistaken for correlated crosstalk events, but for operating conditions with typical DCR values of 10 kHz, the probability of a dark count at any given pixel with a particular 10 ns interval is only  $10^{-4}$ .

We have applied this crosstalk evaluation method using two approaches. In the first case, we rely on the DCR data and look for correlations within the dark count data. Although dark counts at any given pixel are very infrequent, if we can assume that the crosstalk behavior at all locations in the array is identical, then a statistical summary based on all dark count primary avalanches, regardless of pixel location, should provide a good assessment of the crosstalk. In the second case, we illuminate a single pixel with a single photon per frame and then look for correlated crosstalk events related to this optically induced primary avalanche. The use of optical pulses to induce the primary avalanche is more efficient since it occurs at the same pixel in every frame, and pixel data is required for a much smaller area than the entire array—e.g., we have determined that crosstalk contributions outside a  $9 \times 9$  sub-array with the primary avalanche at the center are insignificant. We have confirmed that we obtain identical results for both approaches. [4]

The definition of appropriate metrics for quantifying crosstalk in GmAPD FPAs has not yet reached a broad consensus. It is straightforward from the analysis just described to compute the probability of a crosstalk event for any given neighboring pixel with a specific geometric relationship to the primary avalanche pixel, but it is not clear how useful this is for end users with particular application objectives. Recent work by Younger, et al. at MIT Lincoln Laboratory [21] includes a useful discussion of crosstalk quantification and the proposal of two system-applicable figures of merit. They define the expected number of correlated crosstalk counts  $E(n)$  within a specified distance and time interval. (As just mentioned, we have found that a  $9 \times 9$  sub-array and a time interval of 10 ns captures essentially all crosstalk events in our FPAs.) Additionally, they propose that the probability  $P(n>1)$  of correlated crosstalk avalanches occurring at more than one nearby pixel is a useful figure of merit since the occurrence of just a single crosstalk event is often tolerable for system designers, but two or more events causes significant performance degradation. We also report the related probability  $P(n=1)$  that exactly one correlated crosstalk event occurs, as well as the total probability  $P(\text{tot})$  for all crosstalk events (for which  $n$  can be 1 or more).

## 4.2 Crosstalk analysis results

Using the analysis approach just described above, we illustrate in Figure 9(a) the dependence of the crosstalk probability per pixel on the distance between the primary (optically induced) avalanche and the correlated crosstalk avalanche in units of the pixel pitch (i.e.,  $100 \mu\text{m}$ ). For instance, data points for a distance of 1 pixel correspond to the four nearest neighbors (up, down, right, and left), and data points for a distance of  $\sim 1.4$  pixels correspond to next-nearest neighbors in the four diagonal directions. Results are presented for two typical pixels at operating conditions corresponding to PDE values of 30 – 35%. The patterns observed in this plot are similar for both pixels and have been found to be a reproducible signature [4] dictated by the geometric structure of our GmAPD PDAs.

In Figure 9(b), we present an analysis of the same data set from which we can plot the probability of a particular number of crosstalk events occurring in response to a primary avalanche. The figure of merit described above for the probability of more than one crosstalk event,  $P(n>1)$ , was found to be just over 2%, and the average expected number of crosstalk counts per primary avalanche  $E(n)$  is 0.16.

The analysis described thus far includes all crosstalk events occurring within 10 ns of the primary avalanche, and for longer time delays than this, we find a negligible contribution. It is also possible to analyze the distribution of these crosstalk events with respect to the time delay. We find that  $\sim 92\%$  of the crosstalk events occur within 2 ns of the primary avalanche and that  $\sim 98\%$  of the crosstalk events occur within 5 ns of the primary avalanche.

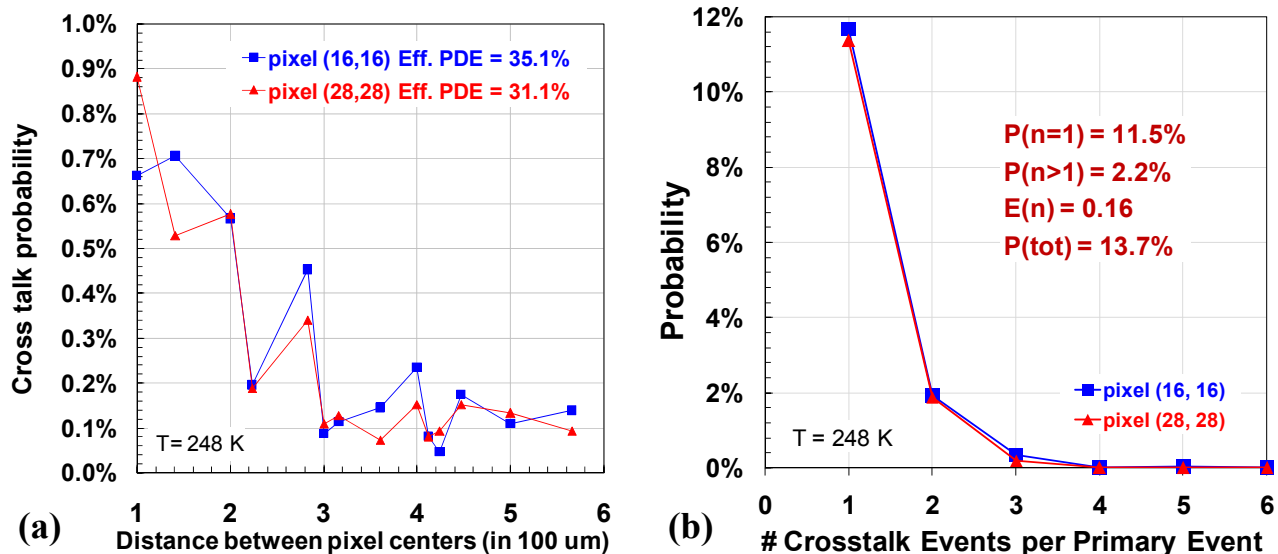


**Figure 9.** Results of crosstalk analysis for FPA operated at 248 K and 3.25 V excess bias, corresponding to an average PDE of  $\sim 31\%$  (see Figure 6). Analysis was carried out using 10,000 frames of data obtained for  $9 \times 9$  regions with the center pixel illuminated to initiate a primary avalanche event. In (a), the crosstalk probability per pixel is plotted as a function of the distance of the pixel from the primary avalanche (in multiples of the  $100 \mu\text{m}$  pixel pitch). The probability for various crosstalk metrics are computed from the results in (b), which indicate the probabilities for a specific number of crosstalk events occurring in response to a primary avalanche event.

## 5. CHARACTERIZATION OF TIMING JITTER

### 5.1 Jitter measurement technique using over-sampling

In any LADAR system, the accuracy with which the range of an object can be determined is limited by the total uncertainty in the measurement of the roundtrip time-of-flight between the sensor and the object. The contribution of the FPA to this total uncertainty, commonly referred to as the timing jitter, is an important characteristic of the FPA performance. For optical pulses that nominally arrive at the FPA at precisely the same time within successive range gates, an FPA with perfect timing characteristics will always register a count in the same time bin (i.e., with the same timestamp). However, finite timing jitter can cause counts to occur in different bins from one frame to the next.

To characterize the jitter of our GmAPD FPAs, we have employed an over-sampling technique that is similar to approaches used with digital sampling oscilloscopes and eye-diagram analyzers for communications links. In Figure 10(a), we present a simple illustration of the concept. The top panel shows the response of the FPA with a nominal photon arrival occurring precisely in the center of time bin  $N$ . Although most counts are registered in time bin  $N$ , the finite timing jitter of the FPA causes some fraction of the counts to register in time bins  $N-1$  and  $N+1$ , indicated by solid red circles. The lower panel illustrates a second set of measurements with the nominal photon arrival shifted by 2.5 time bins, in which case most counts occur in either of time bins  $N+2$  and  $N+3$ , but some occur in  $N+1$  and  $N+4$ , as indicated by open green circles. The basic premise of the over-sampling analysis is to shift the data for the second set of measurements by a temporal offset that is exactly equal and opposite to the shift in the photon arrival time (i.e., 2.5 time bins in this example). After shifting the second set of measurements to the solid green circles, the combination of the solid red and green circles comprises a more detailed description of the timing probability distribution function (PDF). In the simple example illustrated by Figure 10(a), just two different photon arrival times are used, but the same principle can be applied for a larger number of time shifts to construct a more detailed PDF.

### 5.2 Results of timing jitter characterization

To employ the over-sampling technique just described, we used up to 14 time shifts of 64 ps each by introducing reproducible delays in the drive signal to the pulsed laser. Therefore, for each successive time shift, the laser pulse arrived with successive 64 ps delays relative to the beginning of each range gate. This allowed us to step the photon

arrival through several adjacent time bins, and the nominal photon arrival times occurred at different points within these time bins. By “folding back” the data sets obtained for the delayed photon arrivals by the corresponding time shift used for each set, we obtained the PDF illustrated by the blue data points in Figure 10(b). The solid red curve is the moving average of the individual data points with averages taken for groups of eight successive data points. In addition to the inherent timing jitter of the FPA, the measured PDF includes other sources of timing uncertainty in our test set. The dominant contribution to this test system jitter was the 170 ps full-width at half-maximum (FWHM) of our laser pulses. To determine the timing jitter of the FPA itself, it was necessary to compensate for the contribution of this system jitter.

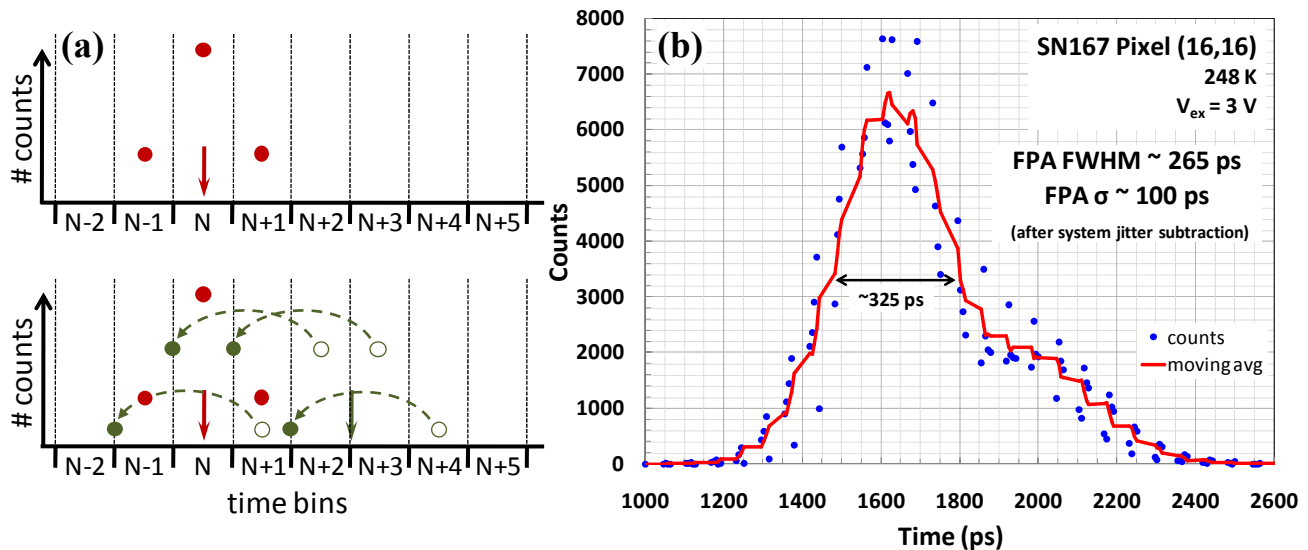


**Figure 10.** (a) Illustration of timing jitter measurement technique. In the top panel, photon arrivals at the center of time bin N (on average) give a count distribution indicated by solid red circles, with counts occurring in time bins N-1, N, and N+1. In bottom panel, photon arrivals have been shifted by exactly 2.5 time bins to coincide (on average) with the boundary between time bins N+2 and N+3, and time bin counts are shown by open green circles. To combine all data to form an oversampled probability distribution function (PDF), the second set of measurements is shifted by the initial 2.5 time bin arrival offset (as shown with dashed arrows) to plot the solid green circles. (b) Experimental results using technique described in (a) with 14 incremental photon arrival offsets of 64 ps each. The resulting direct measurement of the timing jitter PDF includes other sources of ~170 ps system timing jitter. After subtraction of system contributions, the FPA PDF is found to have a standard deviation of ~100 ps and a full-width half-maximum of ~265 ps.

Based on the moving average, the PDF has a FWHM of ~325 ps, and after correction for the measurement system-level jitter, the FPA timing jitter as determined by a FWHM criterion was ~265 ps. Because the FWHM criterion does not capture non-Gaussian features of the full PDF, such as the apparent tail on the right side of our measurement distribution, the standard deviation of the entire measured PDF is often a preferred metric for the timing jitter. The computed standard deviation of the blue data points is ~100 ps.

The timing jitter of the FPA has two primary contributions: the detection process of the GmAPD and the electronic circuitry of the ROIC. The GmAPD itself has uncertainty in its response to a photon arrival, and this was independently characterized on discrete detectors fabricated on the same wafers with the PDAs used to build the FPAs described here. For equivalent excess biases of ~3 V, the timing jitter of these discrete detectors was found to be about 100 ps (FWHM criterion), in reasonable agreement with past results for GmAPDs of a similar design. [5] This means that the majority of the measured 265 ps timing jitter (FWHM) originates in the various circuit elements of the ROIC.

## 6. CONCLUSIONS

We have described 32 x 32 FPAs based on GmAPDs with single photon sensitivity developed for 3-D LADAR imaging applications at 1.06  $\mu\text{m}$ . Performance mapping for DCR and PDE across the entire 100  $\mu\text{m}$  pitch array shows excellent yield, including 100% hybridization connectivity, with just a single pixel exhibiting high DCR. All other 1023 pixels have less than 26 kHz DCR, with an average value of 15 kHz, for an array-level average PDE of 35% with the FPA

operating at 248 K and 3.5 V excess bias. Pixel-level characterization the DCR vs. PDE tradeoff shows that the average pixel achieves 40% PDE with 20 kHz DCR at 248 K. The ROIC design permits very high frame rates of up to 186 kHz with 2  $\mu$ s range gates, and range gates can be set to any duration between 1 ns and 2  $\mu$ s.

Crosstalk characterization shows a distinctive signature for the crosstalk probability at different pixels near the primary avalanche pixel, with nearest neighbor pixels exhibited just below 1% crosstalk probability. The integrated crosstalk for all pixels within a 9 x 9 sub-array surrounding the primary avalanche pixel and for time delays as long as 10 ns is about 14%; crosstalk at larger distances and longer temporal delays was found to be negligible. The probability of more than one correlated crosstalk event occurring per primary avalanche was on the order of 2%, and the expected number of crosstalk counts per primary avalanche was 0.16. The timing jitter behavior of the FPA was characterized using an over-sampling technique that permitted direct measurement of the timing probability distribution function. The FPA timing PDF exhibited a FWHM of 265 ps and a standard deviation of 100 ps.

Many elements of the FPA design—including GmAPD structure, ROIC architecture, and packaging platforms—have been defined to be forward-compatible with next generation 32 x 128 FPAs with 50  $\mu$ m pitch. Prototypes of these new FPAs are currently in evaluation.

## ACKNOWLEDGMENTS

We are grateful to Dr. Monte Turner for his support throughout this work, for which we acknowledge funding from DARPA. We also greatly appreciate the collaborative efforts of many colleagues at MIT Lincoln Laboratory, including Gary Smith, Alex McIntosh, Simon Verghese, Brian Aull, Brian Tyrrell, and Joe Funk.

## REFERENCES

- [1] M. A. Albota, B. F. Aull, D. G. Fouche, *et al.*, “Three-dimensional imaging laser radars with Geiger-mode avalanche photodiode arrays,” *MIT Lincoln Laboratory Journal*, vol. 13, no. 2, p. 351 – 370 (2002).
- [2] B. F. Aull, A. H. Loomis, D. J. Young, *et al.*, “Three-dimensional imaging with arrays of Geiger-mode avalanche photodiodes,” *Proceedings of the SPIE* 5353, p. 105 – 116 (2004).
- [3] B. F. Aull, A. H. Loomis, D. J. Young, R. M. Heinrichs, B. J. Felton, P. J. Daniels, D. J. Landers, “Geiger-mode avalanche photodiodes for three-dimensional imaging,” *MIT Lincoln Laboratory Journal*, vol. 13, no. 2, p. 335 – 350 (2002).
- [4] M. A. Itzler, M. Entwistle, M. Owens, X. Jiang, K. Patel, K. Slomkowski, T. Koch, S. Rangwala, P. F. Zalud, Y. Yu, J. Tower, J. Ferraro, “InP-based Geiger-mode avalanche photodiode arrays for three-dimensional imaging at 1.06  $\mu$ m,” *Proceedings of the SPIE* 7320, 7320-00 (2009).
- [5] M. A. Itzler, R. Ben-Michael, C.-F. Hsu, K. Slomkowski, A. Tosi, S. Cova, F. Zappa, and R. Ispasoiu, “Single photon avalanche diodes (SPADs) for 1.5  $\mu$ m photon counting applications”, *J. Mod. Opt.*, vol. 54, no. 2-3, pp. 283-304 (2007).
- [6] M. A. Itzler, X. Jiang, R. Ben-Michael, K. Slomkowski, M. A. Krainak, S. Wu, and X. Sun, “InGaAsP avalanche photodetectors for non-gated 1.06  $\mu$ m photon-counting receivers,” *Proceedings of the SPIE* 6572, 65720G (2007).
- [7] X. Jiang, M. A. Itzler, R. Ben-Michael, K. Slomkowski, “InGaAsP/InP Avalanche Photodiodes for Single Photon Detection”, *IEEE J. of Sel. Topics in Quantum Electronics* 13, p. 895 – 905 (2007).
- [8] X. Jiang, M. A. Itzler, R. Ben-Michael, K. Slomkowski, “InGaAsP avalanche photodetectors for near IR single photon detection,” *Proceedings of the SPIE* 6771, 677127 (2007).
- [9] X. Jiang, M. A. Itzler, R. Ben-Michael, K. Slomkowski, M. A. Krainak, S. Wu, and X. Sun, “Afterpulsing effects in free-running InGaAsP single photon avalanche diodes,” *IEEE J. Quantum Electron.*, vol. 44, p. 3 – 11 (2008).
- [10] M. A. Itzler, X. Jiang, R. Ben-Michael, B. Nyman, K. Slomkowski, “Single Photon Avalanche Diodes for Near-Infrared Photon Counting,” *Proceedings of the SPIE* 6900, 6900-48 (2008).
- [11] K. Nishida, K. Taguchi, and Y. Matsumoto, “InGaAsP heterostructure avalanche photodiodes with high avalanche gain,” *Appl. Phys. Lett.*, vol. 35, 251–252 (1979).
- [12] J. C. Campbell, A. G. Dentai, W. S. Holden, and B. L. Kasper, “High-performance avalanche photodiode with separate absorption, ‘grading’, and multiplication regions,” *Electron. Lett.*, vol. 19, 818 – 820 (1983).
- [13] S. R. Forrest, O. K. Kim, and R. G. Smith, “Optical response time of In<sub>0.53</sub>Ga<sub>0.47</sub>As avalanche photodiodes,” *Appl. Phys. Lett.*, vol. 41, 95–98 (1982).
- [14] Y. Liu, S. R. Forrest, J. Hladky, M. J. Lange, G. H. Olsen, D. E. Ackley, *J. Lightwave Tech.*, vol. 10, 182 (1992).
- [15] M. A. Itzler, K. K. Loi, S. McCoy, N. Codd, N. Komaba, “High-performance, manufacturable avalanche photodiodes for 10 Gb/s optical receivers,” *Proc. of 25<sup>th</sup> Optical Fiber Communication Conference (OFC 2000)*, Vol. 4, p. 126–128 (2000).
- [16] K.A. McIntosh, J. P. Donnelly, D.C. Oakley, *et al.*, “InGaAsP/InP avalanche photodiodes for photon counting at 1.06  $\mu$ m,” *Appl. Phys. Lett.*, vol. 81 2505-2507 (2002).

- [17] J. P. Donnelly, E. K. Duerr, K. A. McIntosh, *et al.*, "Design Considerations for 1.06- $\mu\text{m}$  InGaAsP-InP Geiger-Mode Avalanche Photodiodes," *IEEE J. Quantum Electron.*, vol. 42, 797-809 (2006).
- [18] S. Verghese, J. P. Donnelly, E. K. Duerr, *et al.*, "Arrays of InP-based Avalanche Photodiodes for Photon Counting," *IEEE Sel. Topics in Quantum Electron.* vol. 13, p. 870 – 886 (2007).
- [19] R. Sudharsanan, P. Yuan, J. Boisvert, P. McDonald, T. Isshiki, S. Mesropian, E. Labios, "Single photon counting Geiger mode InGaAs(P)/InP avalanche photodiode arrays for 3D imaging," *Proceedings of the SPIE* 6950, 69500N (2008).
- [20] P. Yuan, R. Sudharsanan, X. Bai, J. Boisvert, P. McDonald, E. Labios, M. S. Salisbury, G. M. Stuart, H. Danny, A. A. Portillo, A. B. Roybal, S. Van Duyne, G. Pauls, S. Gaalema, "32 x 32 Geiger-mode LADAR Cameras," *Proceedings of the SPIE* 7684, 76840C (2010).
- [21] R. D. Younger, K. A. McIntosh, J. W. Chludzinski, D. C. Oakley, L. J. Mahoney, J. E. Funk, J. P. Donnelly, S. Verghese, "Crosstalk Analysis of Integrated Geiger-mode Avalanche Photodiode Focal Plane Arrays," *Proceedings of the SPIE* 7320, 73200Q (2009).